

Using finite element simulations to optimise metal machining

The majority of metal-cutting operations involve the creation of chips from the workpiece. Prediction of chip form is important because chip form directly influences surface finish and may lead to damage of the machined surface, the cutting tool or the machine. The finite element method (FEM) may be used to simulate chip formation quite precisely and this note shows how the method may be applied. The mathematics involved is outlined in Appendices, which may look complex. If maths is not your thing, you may want to review the simulation results only.



Depending on the workpiece material and the cutting conditions, you will see that three type of chips (continuous, serrated, and discontinuous) may be produced during metal machining. As the simulations will demonstrate, the type of chip is influenced by tool rake angles, cutting speeds, and depth of cut. The numerical results obtained in our simulation are compared with experimental data collected from literature wherever possible. You will read that good overall agreement is found.

Keywords: chip formation, tool-rake angle, cutting speed, depth of cut, Titanium alloy

1. Introduction

Machining (turning, drilling, milling, boring, etc.) is one of the most popular and oldest manufacturing operations. It is reported that approximately 15% of the value of all mechanical components produced in the world comes from the machining process [1]. Because chip formation is one of fundamental features of the metal cutting process, understanding the mechanics of chip formation is essential for designing more effective tools and enhancing the efficiency of machining operations. Many analytical, empirical, and numerical models have been developed since the 19th century [2].

The analytical and empirical models have made significant contribution to the field by providing information about chip formation process. However, most of the theories were based on simple observations of metal cutting which led to the development of the 2D orthogonal metal cutting model as shown in Figure 1. The 2D model and its idealised form have a number of drawbacks. For example, the model's material behaviour is unrealistic and misrepresents contact condition between the tool and workpiece. Although there have been attempts to extend such results to 3D oblique cutting model, the oversimplified analytic approach still lacks predictability of the complex metal cutting process and the need for numerical analysis is indisputable [3].

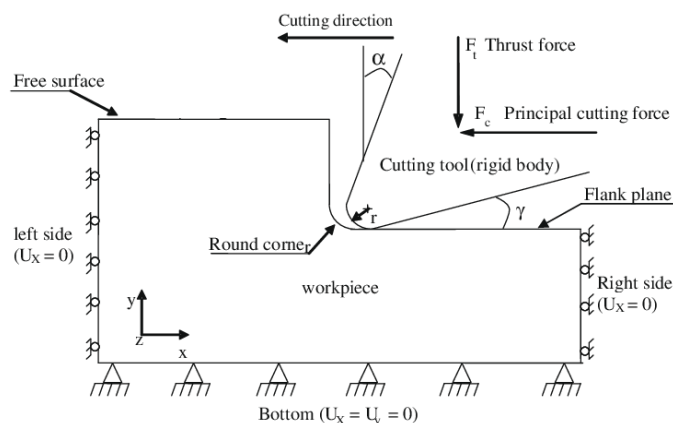


Figure 1: Schematic view of the orthogonal metal cutting model, showing the tool geometry, workpiece, and boundary condition where α is the tool rake angle, γ the tool flank angle, and r the tool edge radius [4].

Since the development of finite element method (FEM) in the early 1970s, numerical simulation of this process has become increasingly more popular due to its ability to provide detailed insight into the process. FEM has been widely used to evaluate chip formation processes in relation to operating parameters, tool settings, and material properties. Such simulations have reduced costly experimental tests and prototyping used in tool and process designs. An example of a FEM model setup is shown in Figure 2.

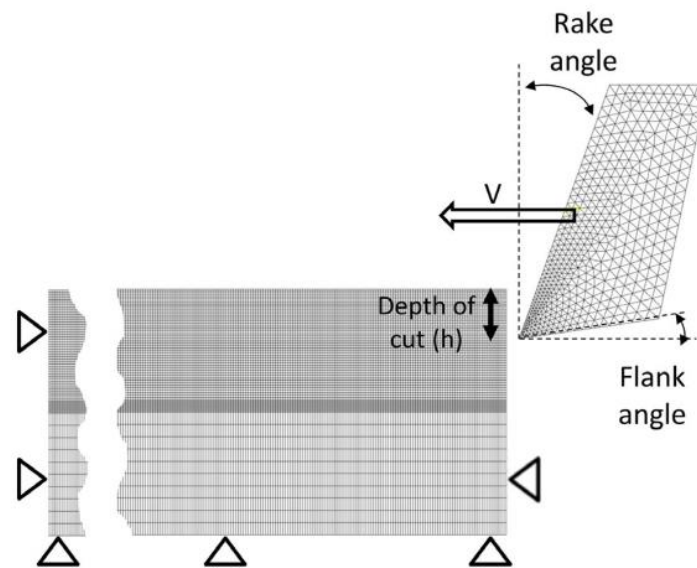


Figure 2: A 2D example of tool and workpiece setup used in FEM modelling. V is the cutting tool speed and h is depth of cut.

2. FEM simulations

2.1 Material property

In this note, the machining of the most common Titanium alloy (Ti-6Al-4V) is selected for investigation. Ti-6Al-4V is an important aerospace engineering material because it provides a good combination of mechanical resistance and fracture toughness, along with low density and excellent resistance to corrosion. The cutting insert is made of Tungsten Carbide (WC ISO-P20). Johnson-Cook and Hillerborge material parameters of the workpiece may be found in Table 1 and the physical parameters of both the workpiece and the tool-insert are provided in Table 2.

Table 1: Johnson-Cook and Hillerborge material parameter values of Ti-6Al-4V.

A (MPa)	B (MPa)	n	C	m	D_1	D_2	D_3	D_4	D_5	$\dot{\epsilon}_0$
1,098	1,092	0.93	0.14	1.1	-0.09	0.25	-0.5	0.014	3.87	1

Table 2: Mechanical and thermophysical parameters of workpiece and tool.

Physical parameters	Workpiece (Ti-6Al-4V)	Tool (WC ISO-P20)
Density, ρ (kg/m ³)	4,430	15,700
Elastic modulus, E (GPa)	110	705
Poisson's ratio, ν	0.342	0.23
Specific heat, C_p (J/kg°C)	670	178
Thermal conductivity, λ (W/m°C)	6.6	24
Expansion coefficient, α_d ($\mu\text{m}/\text{m}/^\circ\text{C}$)	9	5
T_{melt} ($^\circ\text{C}$)	1630	-
T_{room} ($^\circ\text{C}$)	25	25

2.2 Chip classification

During machining operations, three classes of chip may occur: continuous chips, serrated chips, and discontinuous chips. These are illustrated in Figure 3.

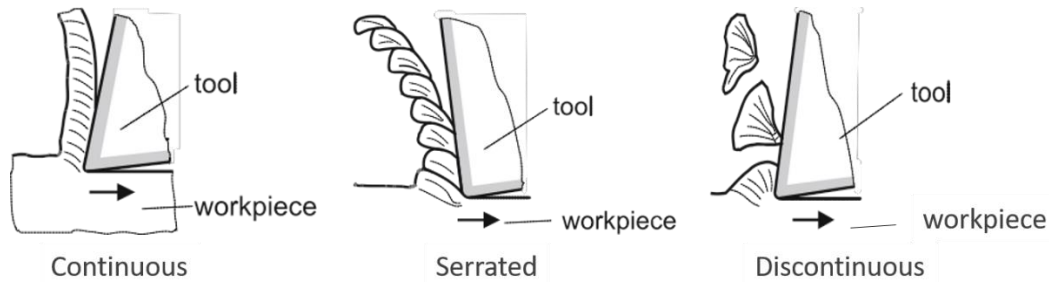


Figure 3: Chip shapes.

While continuous chip is often considered as an ideal chip that generates stable cutting forces, it is not desired for automated machining. This is because the continuous chip may damage the machined components, the cutting tools, and clog the machine. To overcome these issues, serrated chips may be considered because they are easy to break during machining. Removing serrated chips is also easier than removing continuous chip.

2.3 Benchmark test (BMT)

We will compare the accuracy of the numerical method, with the benchmark test (BMT) of machining Ti-6Al-4V presented in [1]. Our numerically generated images will also be compared with the experimental chip, wherever possible.

2.3.1 BMT simulation setup

Two benchmark tests using different cutting speeds, V , of 60 m/s (BMT-1) and 180 m/s (BMT-2) are available for comparative purposes. The cutting and boundary conditions in our simulation are described in Figure 1, which is made the same as the experiment setup. The carbide tool geometry is defined by a -4° rake angle (α) over 0.15mm, a 7° flank angle (γ), and a $20\ \mu\text{m}$ tip radius (r) as shown in Figure 4. The cutting depth, h , is set at $100\ \mu\text{m}$. The Coulomb friction coefficient of 0.2 is applied between the tool and workpiece.

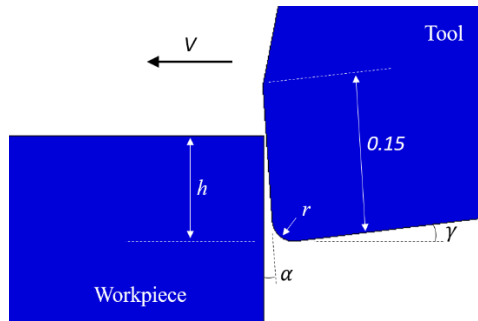


Figure 4: Tool geometry and cutting setup.

2.3.2 BMT numerical results

Figures 5 and 6 show the chips generated from the experiment and simulation. The chip morphology is described by tooth width (L_t), the minimum (h_1) and maximum (h_2) tooth height. Table 3 compares the results obtained from the experiment and the FEM simulation. We can see that the numerical results are in good agreement with the experimental ones.

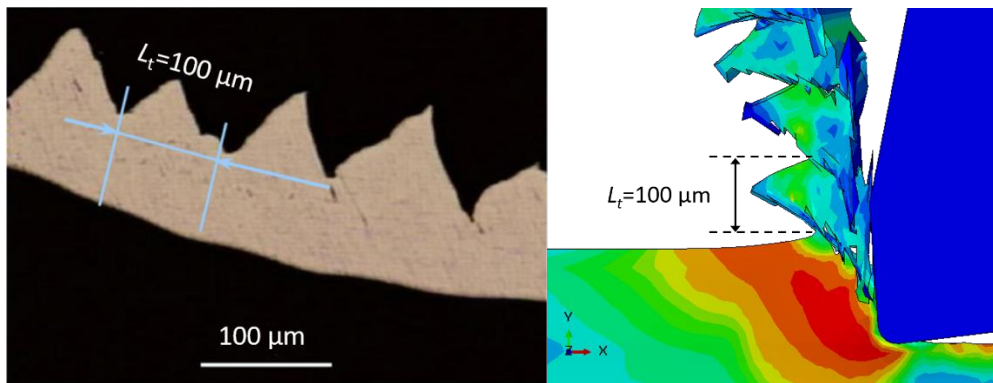


Figure 5: BMT-1: $v = 60 \text{ m/min}$, $h = 100 \mu\text{m}$, $\alpha = -4^\circ$, and $\gamma = 7^\circ$. Comparison of real chip (left) and simulated chip (right).

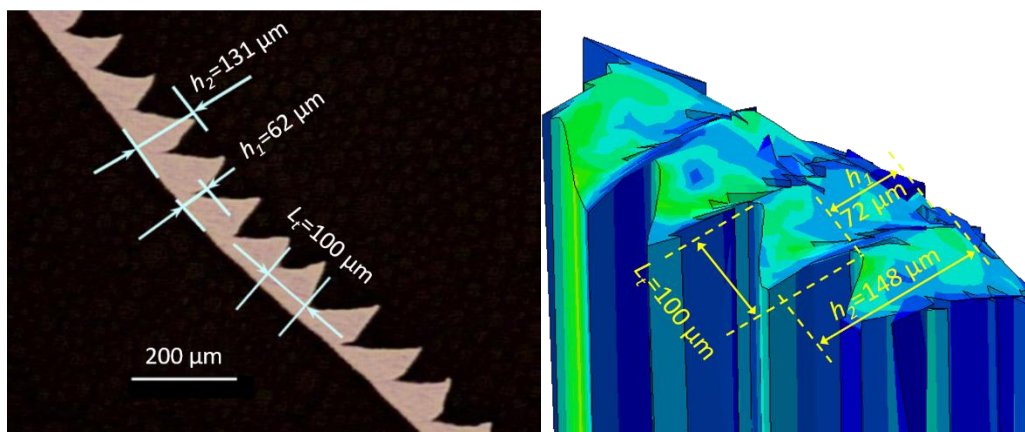


Figure 6: BMT-2: $v = 180 \text{ m/min}$, $h = 100 (\mu\text{m})$, $\alpha = -4^\circ$, and $\gamma = 7^\circ$. Comparison of real chip (left) and simulated chip (right).

Table 3: Result comparisons between experiment and simulation in the two benchmark tests.

Test cases		L_t (μm)	h_1 (μm)	h_2 (μm)
BMT-1	Experiment	100	-	-
	Simulation	100	-	-
BMT-2	Experiment	100	62	131
	Simulation	100	72	148

Clearly, the numerical model has shown its suitability for predicting chip formation characteristics. We will investigate the effects of depth of cut, rake angle, and cutting speed on chip characteristics in the following sections. It is noted that all parameters used in BMT-1 will be used in the simulations.

2.4 Influence of depth of cut on chip type

The depth of cut is one of the more influential parameters for the determination of chip form, as demonstrated in the simulations present in Figure 7. This figure shows that continuous chips are generated when the depth of cut is reduced to 50 and 20 μm . In contrast, serrated chips were observed in the BMT-1 with the depth of cut $h = 100 \mu\text{m}$. When the depth of cut is increased to $h = 150 \mu\text{m}$, discontinuous chips are produced.

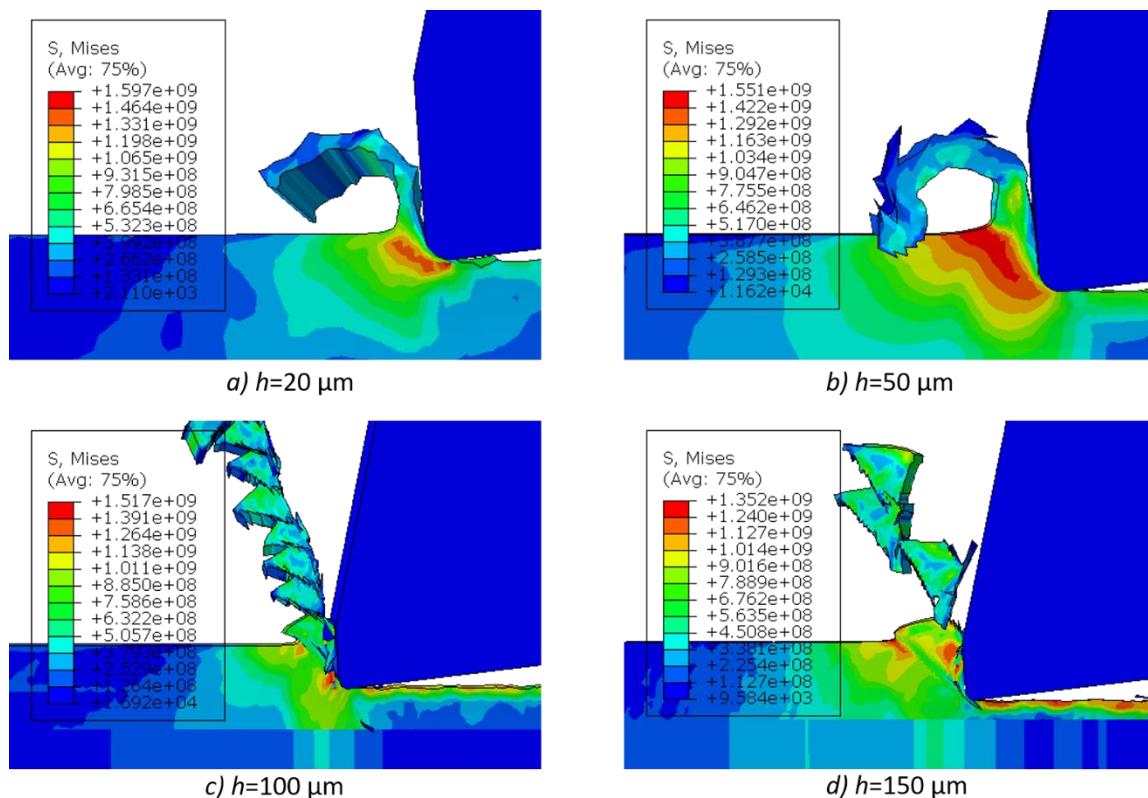


Figure 7: $V = 60 \text{ m/min}$, $\alpha = -4^\circ$, and $\gamma = 7^\circ$; a) $h = 20 \mu\text{m}$, b) $h = 50 \mu\text{m}$, c) $h = 100 \mu\text{m}$, and d) $h = 150 \mu\text{m}$. Continuous chips are produced for both cases a) and b), serrated chips for c), and discontinuous chips for d).

2.5 Influence of rake angle on chip formation

The formation of continuous, serrated, and discontinuous chips are also influenced by the tool rake angle. The FEM simulation results shown in Figure 8 indicate that negative angles tend to produce discontinuous chips while positive angles result in continuous chip formation. Serrated chips can be obtained within the middle range of the tool rake angles.

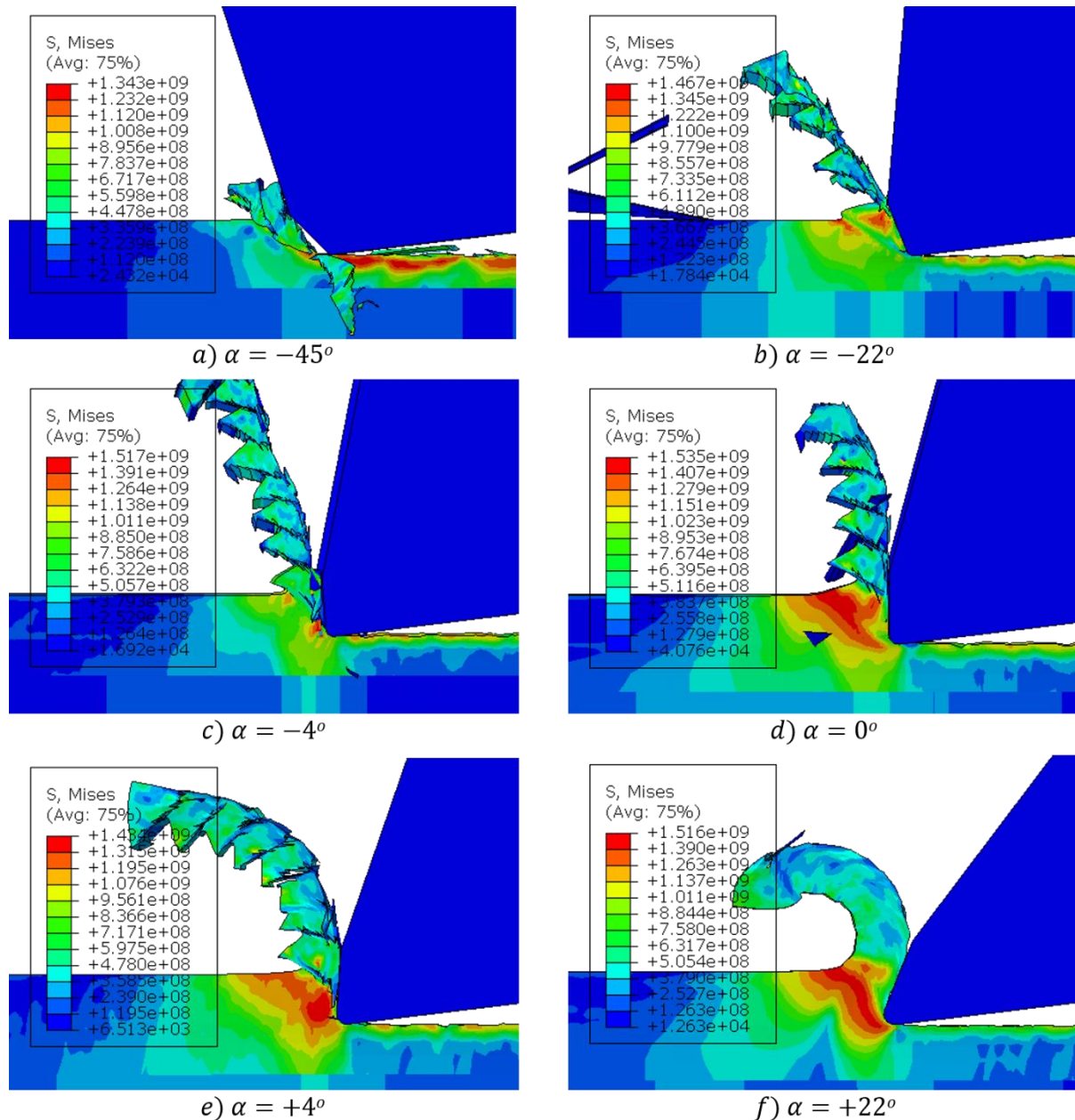


Figure 8: $V = 60$ m/min, $h = 100$ μ m, and $\gamma = 7^\circ$; a) $\alpha = -45^\circ$, b) $\alpha = -22^\circ$, c) $\alpha = -4^\circ$, d) $\alpha = 0^\circ$, e) $\alpha = +4^\circ$, and f) $\alpha = +22^\circ$. Discontinuous chips are produced for cases a), serrated chips for b) to e), and continuous chips for f).

2.6 Influence of cutting speed on chip type

In the BMT tests, serrated chips were generated as shown in Figures 5 and 6 (at cutting speeds of $V=60$ m/s for BMT-1 and $V=180$ m/s for BMT-2). Via an FEM simulation we can see how cutting speed influences chip formation and provide examples for $V=540$ m/s and 1,620 m/s. Figure 9 shows that discontinuous chips are predicted at the higher cutting speeds.

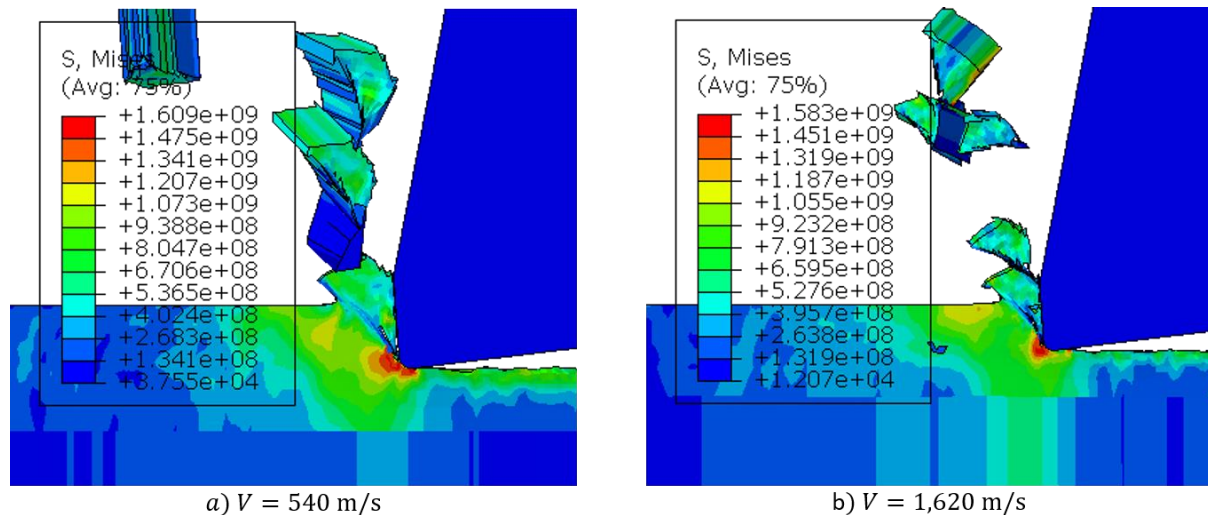
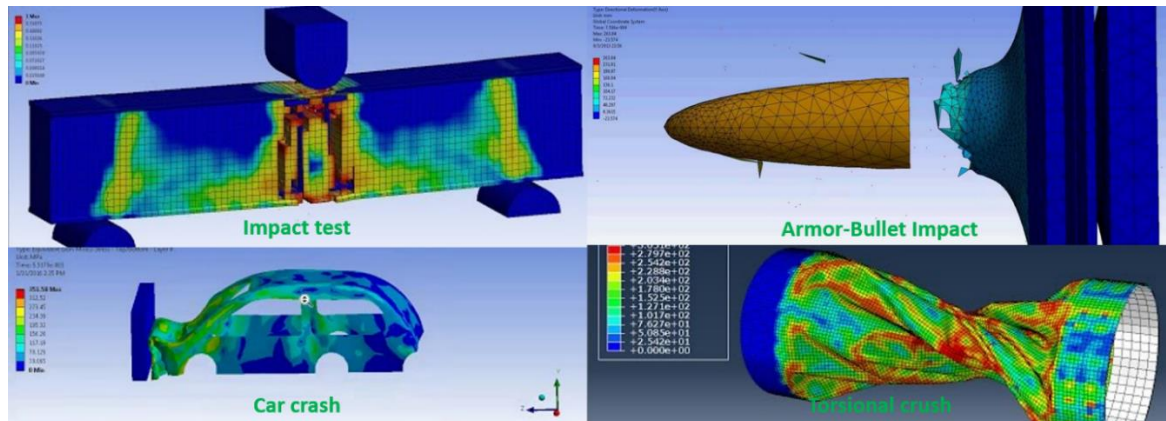


Figure 9: $\alpha = -4^\circ$, and $\gamma = 7^\circ$; $h = 100 \mu\text{m}$; a) $V = 540$ m/s and b) $V = 1,620$ m/s. Discontinuous chips are produced for both cases.

3. Conclusions

As confirmed by experimental results obtained from published literature, our FEM simulations accurately predict chip form and allow the effects of parameters influencing chip formation to be studied. Given the material properties of the workpiece, adjusting the cutting conditions in the simulation (e.g. depth of cut, cutting speed, and tool rake angle) enables prediction of the resultant chip form. It is therefore possible to predetermine the cutting parameters required to produce the serrated chip form preferred for automated machining.

In our simulations, the Johnson-Cook model is used in combination with the Johnson-Cook damage initiation model as well as the Hillerborge damage evolution criteria. These FEM simulation methods may also be used for cost effectively investigating other damage situations as shown below.



In addition to the physical characteristics of chip formation and similar damage processes, parameters such as stress, strain, strain rate and temperature rise, can be determined by finite element simulation. Especially with processes taking place within very short or very long time intervals, such parameters may be difficult, impractical or expensive to measure experimentally.

When detailed information about a physical process is required, but is difficult or expensive to obtain from actual testing, the feasibility of simulating the process using the finite element method should be considered.

Appendices:

A. Johnson-Cook model

Among several constitutive models used in metal cutting simulations, the Johnson-Cook (J-C) [5] has been the most common and available in most of the commercial FEM software. It provides a satisfactory description of material behaviour undertaking large strains, at high strain rates and at high temperatures. The J-C method describes the equivalent flow stress of a material by the following equation:

$$\bar{\sigma} = \underbrace{[A + B(\bar{\epsilon})^n]}_{\text{strain-hardening term}} \underbrace{\left[1 + C \ln\left(\frac{\dot{\bar{\epsilon}}}{\dot{\bar{\epsilon}}_0}\right)\right]}_{\text{strain-rate term}} \underbrace{\left[1 - \left(\frac{T - T_{room}}{T_{melt} - T_{room}}\right)^m\right]}_{\text{thermal-softening term}}, \quad (1)$$

where $\bar{\sigma}$ is the equivalent flow stress (MPa), A is the initial yield strength (MPa) of the material at the room temperature, B is the hardening modulus (MPa), $\bar{\epsilon}$ is the equivalent plastic strain, n is the strain-hardening exponent, C is the strain rate factor, $\dot{\bar{\epsilon}}$ is the equivalent plastic strain rate, $\dot{\bar{\epsilon}}_0$ is the reference strain rate, and m is the thermal softening coefficient. T_{room} and T_{melt} represent the room temperature and the melting temperature. The J-C material constants A , B , C , n , and m are experimentally determined in the laboratory.

What is strain hardening? Strain hardening term refers to the strengthening of a metal when its shape is permanently deformed. When the metal is strain-hardened, permanent defects occur within crystal structure of the material. These defects reduce the ability of crystals to move within the metal structure. As a result, the metal's tensile strength and hardness increase and its ductility decreases.

Figure A1 shows what theoretically happens during strain hardening process. A certain amount of strain is put into the material so that it is plastically deformed (grey line). When the load is removed, the material returns to the state of zero stress along a path (purple squares) parallel to the original elastic line. When the material is reloaded, it now follows the new stress-strain curve (blue line). The new stress-strain curve has a new yield strength (green dotted line) which is substantially higher than the original yield strength (red dashed line). However, the original elongation (blue dashed line) has now diminished. The increase in strength will therefore reduce the ductility and formability of the material.

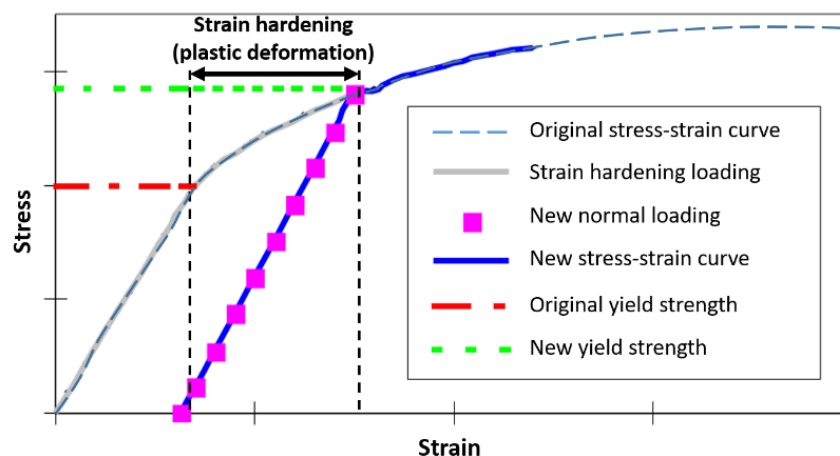


Figure A1: An illustration of stress-strain curve with strain hardening.

What is strain rate? Strain rate is the change in strain (deformation) of a material with respect to time. The strain rate also influences on the tensile strength of the material. Generally speaking the higher the strain rate, the higher the tensile stress becomes. As mentioned earlier, the ductility of the material decreases when the strain rate increases.

What is thermal softening? Thermal softening is the degradation of strength and hardness of a material with increased temperature. Figure A2 shows the effects of strain rate and temperature on the stress-strain curve of a material.

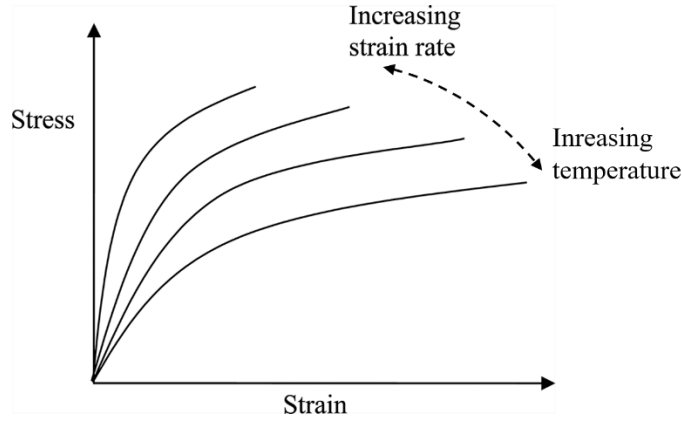


Figure A2: Effects of strain rate and temperature on stress-strain curve.

B. Chip separation criterion

Chip formation can be assumed to occur in two steps before complete ductile failure. The first step is damage initiation and the second one is damage evolution based on the fracture energy approach.

B.1. Damage initiation

The Johnson-Cook damage model [6] is used to simulate damage initiation in conjunction with the J-C flow stress model. In the J-C damage model, the general expression for the equivalent fracture strain is given as follows.

$$\bar{\epsilon}^f = [D_1 + D_2 e^{D_3 \eta}] \left[1 + D_4 \ln \left(\frac{\dot{\epsilon}}{\dot{\epsilon}_0} \right) \right] \left[1 + D_5 \left(\frac{T - T_{room}}{T_{melt} - T_{room}} \right) \right], \quad (2)$$

where $\bar{\epsilon}^f$ is the equivalent plastic strain at failure, η is the triaxiality (a dimensionless ratio of the pressure stress p versus the von Mises stress q , expressed in Equations (3) and (4)) D_1 , is the initial failure strain, D_2 is the exponential factor, D_3 is the triaxiality factor, D_4 is the strain rate factor, and D_5 is the temperature factor. The determination of the five J-C damage parameters ($D_1 \dots D_5$) involves a series of experimental fracture tests, varying the stress triaxiality, strain rate, and temperature. The pressure stress and the von Mises stress are given by

$$p = \frac{\sigma_1 + \sigma_2 + \sigma_3}{3}, \quad (3)$$

$$q = \sqrt{\frac{1}{2}[(\sigma_1 - \sigma_2)^2 + (\sigma_3 - \sigma_2)^2 + (\sigma_1 - \sigma_3)^2]}, \quad (4)$$

where σ_1 , σ_2 , and σ_3 are the three principal stresses. The fracture in a given finite element is initiated when a scalar damage parameter, ω , exceeds unity. This scalar is derived from the following cumulative law

$$\omega = \sum \frac{\Delta \bar{\epsilon}}{\bar{\epsilon}_f}, \quad (5)$$

where $\Delta \bar{\epsilon}$ is the cumulative increment of equivalent plastic strain which is updated at every analysis step. The J-C damage model has been used in numerous applications, including metal cutting problems, because it allows the relatively easy experimental determination of the damage parameters.

B.2. Damage evolution

Figure A3 illustrates characteristics of stress-strain behaviour of a material undergoing damage. The weakening of the material strength shows in two effects: softening of the yield stress and degradation of the elasticity. The solid curve in the figure represents the damaged stress-strain response while the dashed curve is the response without damage. Point B represents the damage initiation point after the strain hardening state (phase A-B). During damage evolution, the load carrying capability of the material reduces until complete failure (phase B-E). The softening response is characterised by a stress-displacement response instead of the stress-strain response. This point will be discussed later.

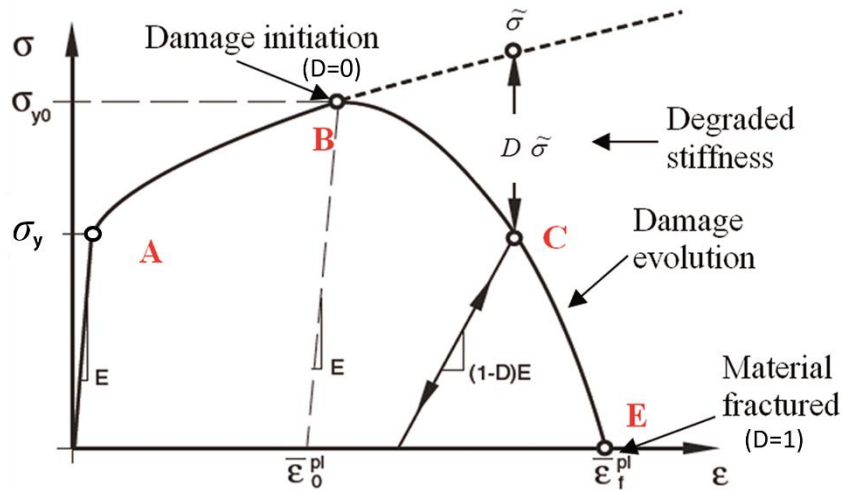


Figure A3: Stress-strain curve with progressive damage degradation [8].

In the figure, σ_{y0} and $\bar{\epsilon}_0^{pl}$ are the yield stress and equivalent plastic strain at the damage initiation and $\bar{\epsilon}_f^{pl}$ is the equivalent plastic strain at failure. The value of $\bar{\epsilon}_f^{pl}$ depends on the characteristic length of the element, L , and cannot be used as a material parameter for the specification of the damage evolution law. Instead, the damage evolution law is specified in terms of equivalent plastic displacement, \bar{u}^{pl} , or in terms of fracture energy dissipation, G_f (Pa). Hillerborg defines the fracture energy, G_f , required to open a unit area of crack as a material property:

$$G_f = \int_{\bar{\epsilon}_0^{pl}}^{\bar{\epsilon}_f^{pl}} L \sigma_y d\bar{\epsilon}^{pl} = \int_0^{\bar{u}_f^{pl}} \sigma_y d\bar{u}^{pl}, \quad (6)$$

where σ_y is the material yield stress (MPa). Before damage initiation $\bar{u}^{pl} = 0$ and after damage initiation $\bar{u}^{pl} = L\bar{\epsilon}^{pl}$. At a given time during the damage evolution, the equivalent plastic stress is calculated by

$$\bar{\sigma} = (1 - D)\tilde{\sigma}, \quad (7)$$

where $\tilde{\sigma}$ is the effective (undamaged) stress computed at the current increment and D is the evolution of damage variable with plastic displacement, which can be specified in linear or exponential forms. The linear evolution law assumes a linear evolution of the damage variable with plastic displacement as

$$D = L\bar{\epsilon}^{pl}/\bar{u}_f^{pl} = \bar{u}^{pl}/\bar{u}_f^{pl}, \quad (8)$$

where the equivalent plastic displacement at failure is

$$\bar{u}_f^{pl} = 2G_f/\sigma_y. \quad (9)$$

The exponential damage evolution law is given by assuming an exponential evolution of the damage variable with plastic displacement as

$$D = \left(1 - e^{-\varphi(\bar{u}^{pl}/\bar{u}_f^{pl})}\right)/(1 - e^{-\varphi}), \quad (10)$$

where φ is the exponent. Figure A4 illustrates the linear and exponential evolution of the damage variable based on plastic displacement.

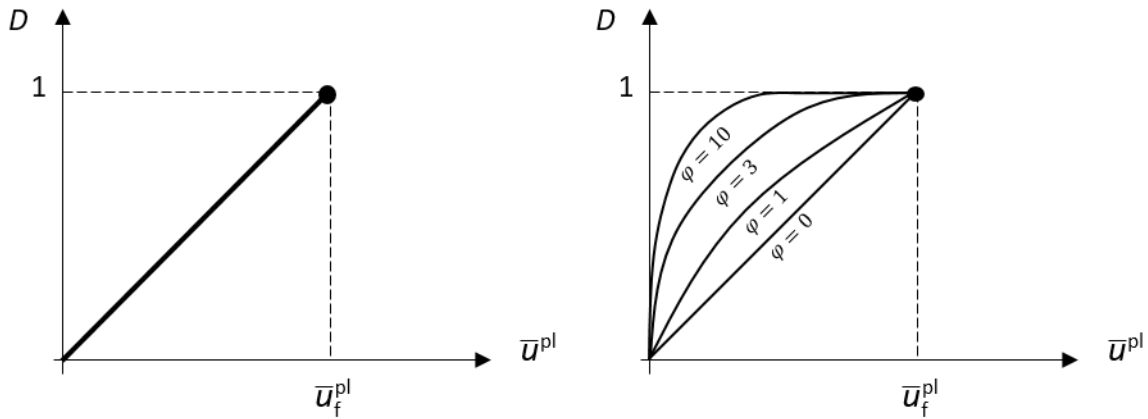


Figure A4: Illustration of linear (left) and exponential (right) evolution of the damage variable.

References:

- [1] Madalina C., Dominique C., and Franck G. (2008). A new material model for 2D numerical simulation of serrated chip formation when machining titanium alloy Ti-6Al-4V, *International Journal of Machine Tools & Manufacture*, 48, 275–288.
- [2] Yalla A., Xinran X., and Viktor P.A. (2011). FEM simulation of metal cutting using a new approach to model chip formation. *International Journal of Advances in Machining and Forming Operations*, 3(2), 71-92.
- [3] Movahhedy M.R., Gadala M.S., and Altintas Y. (2000). Simulation of chip formation in orthogonal metal cutting process: an ALE finite element approach. *Machining Science and Technology*, 4(1), 15-42.
- [4] Lasri L., Nouari M., and Mansori M.E. (2009). Modelling of chip separation in machining unidirectional FRP composites by stiffness degradation concept. *Composites Science and Technology* 69, 684–692.
- [5] Johnson G.R. and Cook W.H. A constitutive model and data for metals subjected to large strains, high strain rates and high temperatures. *Proceeding 7th International Symposium On Ballistics*, Hague, Netherlands, 541-547 (April 1983).
- [6] Johnson G.R., Cook W.H. (1985). Fracture characteristics of three metals subjected to the various strains, strain rates, temperatures and pressures. *Engineering Fracture Mechanics*, 21(1), 31-48.
- [7] Hillerborg A., Modéer M., and Peterson P.E. (1976). Analysis of crack formation and crack growth in concrete by means of fracture mechanics and finite elements. *Cement and Concrete Research*, 6 (6), 773-781.
- [8] Abaqus/Explicit theory and user manuals, Version 6.9. Accessed 5th October 2017.



Sep 2017 by Tri Tien
www.caebay.com
info@caebay.com

Simulations based on engineering integrity
Finite element analysis | Fluid flow simulation
Multibody dynamics | Fluid structure interaction
Discrete element method | Heat transfer

Acknowledgements. The author would like to thank Cliff Walker of Vacmobiles.com for his insightful comments and suggestions that greatly improved the quality of this note. Any errors that remain, of course, are the author's own.

Copyright. CAEbay endeavours to contribute its knowledge towards engineering progress. This note is free for any use, either commercial or educational, that could make products better and safer. However, if published elsewhere, acknowledgement of the source would be much appreciated.

Disclaimer of reliability. The information in this note is correct to the best of our knowledge. However, because material supply and manufacturing quality are outside our control, all recommendations are made without guarantee on the part of the author or CAEbay. The author and CAEbay disclaim any liability in connection with the use of this information.

Feedback or queries on this note? We are keen to improve the accuracy and value of CAEbay's notes. If you have any feedback or queries, please email info@caebay.com. We would be pleased to hear from you!